

# The ESO-VLT MikiS survey reloaded: the internal kinematics of the core of M75<sup>★</sup>

Silvia Leanza<sup>1,2</sup>, Cristina Pallanca<sup>1,2</sup>, Francesco R. Ferraro<sup>1,2</sup>, Barbara Lanzoni<sup>1,2</sup>, Enrico Vesperini<sup>3</sup>, Mario Cadelano<sup>1,2</sup>, Livia Origlia<sup>2</sup>, Cristiano Fanelli<sup>2</sup>, Emanuele Dalessandro<sup>2</sup>, and Elena Valenti<sup>4,5</sup>

<sup>1</sup> Dipartimento di Fisica e Astronomia, Università di Bologna, Via Gobetti 93/2 I-40129 Bologna, Italy

<sup>2</sup> INAF-Osservatorio di Astrofisica e Scienze dello Spazio di Bologna, Via Gobetti 93/3 I-40129 Bologna, Italy

<sup>3</sup> Department of Astronomy, Indiana University, Bloomington, IN, 47401, USA

<sup>4</sup> European Southern Observatory, Karl-Schwarzschild-Strasse 2, 85748 Garching bei Munchen, Germany

<sup>5</sup> Excellence Cluster ORIGINS, Boltzmann-Strasse 2, D-85748 Garching Bei Munchen, Germany

## ABSTRACT

We present the results of a study aimed at characterizing the kinematics of the inner regions of the halo globular cluster M75 (NGC 6864) based on data acquired as part of the ESO-VLT Multi-Instrument Kinematic Survey (MikiS) of Galactic globular clusters. Our analysis includes the first determination of the line-of-sight velocity dispersion profile in the core region of M75. By using MUSE/NFM observations, we obtained a sample of  $\sim 1900$  radial velocity measurements from individual stars located within  $16''$  (corresponding to about  $r < 3r_c$  where  $r_c$  is the estimated core radius of the system) from the cluster center. After an appropriate selection of the most accurate velocity measures, we determined the innermost portion of the velocity dispersion profile, finding that it is characterized by a constant behavior and a central velocity dispersion of  $\sigma_0 \sim 9 \text{ km s}^{-1}$ . The simultaneous King model fitting to the projected velocity dispersion and density profiles allowed us to check and update previous determinations of the main structural parameters of the system. We also detected a mild hint of rotation in the central  $\sim 7''$  from the center, with an amplitude of just  $\sim 1.0 \text{ km s}^{-1}$  and a position angle of the rotation axis of  $\text{PA}_0 = 174^\circ$ . Intriguingly, the position angle is consistent with that previously quoted for the suspected rotation signal in the outer region of the cluster. Taking advantage of the high quality of the photometric catalog used for the analysis of the MUSE spectra, we also provide updated estimates of the cluster distance, age, and reddening.

**Key words.** Globular star clusters: individual (NGC 6864) — Stellar kinematics — Spectroscopy

## 1. Introduction

This paper is part of a long-term project (*Cosmic-Lab*) aimed at using star clusters as natural cosmic laboratories to study stellar evolution, dynamical evolution, and how the properties of the hosted stellar populations evolve with time in high-density environments. Globular Clusters (GCs) are the ideal stellar systems for this kind of investigation since the continuous gravitational interactions among stars typically occur on a timescale shorter than their age. Hence the effects of this internal evolution are expected to leave some signatures on their stellar populations, e.g., via the formation of exotic species like interacting binaries, blue straggler stars (BSSs) and millisecond-pulsars that cannot be explained by standard stellar evolution (see, e.g., Bailyn 1995; Pooley et al. 2003; Ransom et al. 2005; Ferraro et al. 1992, 2003, 2018a).

The approach proposed by *Cosmic-Lab* foresees a comprehensive study of the global properties of each investigated stellar system, including the photometric and chemical characterization of both the normal and the exotic stellar sub-populations hosted in it. The adopted approach can be schematically summarized as follows: (1) the detailed photometric and spectroscopic characterization of the “canonical” sub-populations hosted in the system (see examples in Valenti et al. 2010; Dalessandro et al. 2013a, 2014, 2016, 2022; Saracino et al. 2015, 2019; Ferraro et

al. 1997, 2009a, 2016, 2021; Pallanca et al. 2021; Cadelano et al. 2023; Deras et al. 2024; Origlia et al. 1997, 2002, 2003, 2011, 2013, 2019; Massari et al. 2014; Crociati et al. 2023); (2) the determination of the cluster structural parameters via projected density profiles derived from star counts even for the innermost regions of high-density stellar systems (see, Ibata et al. 2009; Lanzoni et al. 2007, 2010, 2019; Miocchi et al. 2013; Cadelano et al. 2023; Deras et al. 2023); (3) the characterization of any hosted exotic stellar population (see, e.g., Paresce et al. 1992; Ferraro et al. 1999, 2001, 2003, 2009b, 2023a,b; Dalessandro et al. 2008, 2013b; Cadelano et al. 2018, 2020a; Pallanca et al. 2010, 2013, 2014, 2017; Billi et al. 2023); (4) the full kinematic characterization of the detected populations via the construction of velocity dispersion and rotation profiles from line-of-sight velocities and proper motions of individual stars (see examples in Ferraro et al. 2018b; Lanzoni et al. 2013, 2018a,b; Libralato et al. 2018; Raso et al. 2020; Dalessandro et al. 2021; Leanza et al. 2022, 2023; Pallanca et al. 2023).

In this respect the ESO-VLT Multi-Instrument Kinematic Survey (MikiS; Ferraro et al. 2018b,c) has been specifically designed to characterize the kinematical properties of a representative sample of Galactic GCs at different dynamical evolutionary stages, using different spectrographs currently available at ESO. In the context of this survey, the detailed investigation of the almost unexplored innermost cluster regions has been carried out in an ongoing Large Program (106.21N5, PI: Ferraro) that exploits the remarkable performance of the adaptive optics (AO) assisted integral field spectrograph MUSE.

<sup>★</sup> Based on observations collected at the European Southern Observatory, Cerro Paranal (Chile), under Large Programme 106.21N5 (PI: Ferraro).

As part of this project, here we discuss the internal kinematics of the core region of the Galactic GC M75 (NGC 6864). This is a massive system (with  $V$ -band absolute magnitude  $M_V = -8.57$ ) of intermediate/high metallicity ( $[\text{Fe}/\text{H}] = -1.29$  dex; Carretta et al. 2009), and relatively high central density ( $\log(\rho_0/M_\odot \text{ pc}^{-3}) = 4.9$ ; Pryor & Meylan 1993). It is located in the Halo of the Galaxy at a distance  $d \sim 20$  kpc from the Sun, under the assumption of an apparent distance modulus  $(m - M)_V = 17.09$  and a color excess  $E(B - V) = 0.16$  (Harris 1996, 2010 edition). The shape of the BSS radial distribution suggested that this is a dynamically evolved cluster (see Contreras Ramos et al. 2012; Ferraro et al. 2012), and this result was later confirmed by the analysis of the BSS central sedimentation level (Lanzoni et al. 2016): indeed, M75 is the second most dynamically evolved cluster among the approximately 60 stellar systems investigated so far with this method in the Galaxy (Ferraro et al. 2018c, 2020, 2023a) and in the Magellanic Clouds (Ferraro et al. 2019; Dresbach et al. 2022).

## 2. Observations and data reduction

To explore the line-of-sight internal kinematics of the innermost regions of M75, we acquired spectra of resolved stars with the AO-assisted integral-field spectrograph MUSE (Bacon et al. 2010) installed at the Yepun (VLT-UT4) telescope at the ESO Paranal Observatory. MUSE is constituted by a modular structure of 24 identical Integral Field Units (IFUs), and it is available in two configurations: Wide Field Mode (WFM) and Narrow Field Mode (NFM). We adopted the MUSE/NFM configuration, which provides the highest spatial resolution (with a spatial sampling of  $0.025''/\text{pixel}$ ) over a field of view of  $7.5'' \times 7.5''$ . The NFM configuration is equipped with the GALACSI-AO module (Arsenault et al. 2008; Ströbele et al. 2012) and additionally takes advantage of the Laser Tomography AO correction, which is not available in the MUSE/WFM configuration. MUSE/NFM samples the wavelength range from  $4750 \text{ \AA}$  to  $9350 \text{ \AA}$ , with a resolving power  $R \sim 3000$  at  $\lambda \sim 8700 \text{ \AA}$ . The data set was acquired as part of the ESO Large Program ID: 106.21N5.003 (PI: Ferraro), and consists of a mosaic of eight MUSE/NFM pointings in the core region of the cluster, as shown in Fig. 1. A series of three 750 s long exposures were secured for each pointing (see Table 1), with an average DIMM seeing during the observations of  $0.7''$ . A rotation offset of  $90^\circ$  and a small dithering pattern were set between consecutive exposures, in order to remove possible systematic effects and resolution differences between the individual spectrographs. The data reduction was performed by using the standard MUSE pipeline (Weilbacher et al. 2020) through the EsoReflex environment (Freudling et al. 2013). The pipeline first performs bias subtraction, flat field correction, and wavelength calibration for each IFU, then applies the sky subtraction, performs the flux and astrometric calibration, and corrects all data for the heliocentric velocity. Next, a datacube is produced for each exposure by combining the pre-processed data from the 24 IFUs. As the last step, the pipeline combines the datacubes of the multiple exposures of each pointing into a final datacube, taking into account the offsets and rotations between the different exposures.

The mosaic of the reconstructed  $I$ -band images from the stacking of MUSE datacubes is shown in Fig. 1. Each pointing is labeled with a name according to its position with respect to the cluster center: C, E, N, NW, S, SS, SE, and W stand for central, eastern, northern, northwestern, southern, south-southern, south-eastern, and western pointing, respectively. As can be appreci-

**Table 1.** MUSE/NFM data sets for M75

Name	Date	$N_{\text{exp}}$	$t_{\text{exp}}$ [s]
C	2021-08-17	3	750
E	2021-08-17	3	750
S	2021-08-17	3	750
N	2021-08-18	3	750
W	2021-09-19	3	750
SS	2021-09-19	1	750
NW	2022-06-30	3	750
SE	2022-07-03	3	750

**Notes.** For each MUSE/NFM pointing, the table lists the name, execution date, number of exposures ( $N_{\text{exp}}$ ) and exposure time of each frame ( $t_{\text{exp}}$ , in seconds).

ated, the mosaic provides a nice and almost complete sampling of the innermost  $\sim 7''$  radial region of the cluster.

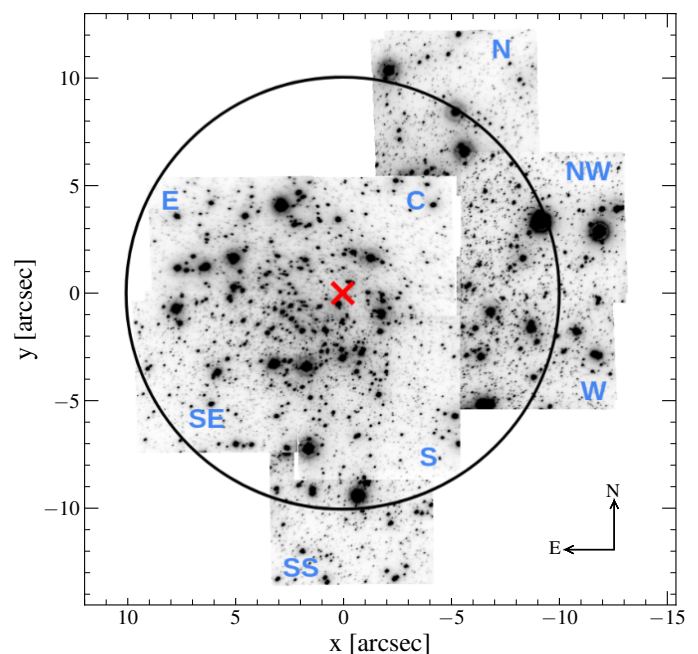


**Fig. 1.** Reconstructed  $I$ -band images of the MUSE/NFM pointings acquired in the core of M75. The circle is centered on the cluster center (red cross, from Contreras Ramos et al. 2012) and has a radius of  $10''$ .

## 3. Analysis

For the extraction of the MUSE spectra we used the software PampelMuse (Kamann et al. 2013), which is designed to extract deblended source spectra of individual stars from observations of crowded stellar regions with integral field spectroscopy, by performing a wavelength-dependent point spread function (PSF) fitting.

### 3.1. The photometric catalog

PampelMuse needs in input the spectroscopic datacube and a photometric reference catalog with the coordinates of the stars

in the datacube field of view, and their magnitudes. We noticed that the photometric catalog presented in Contreras Ramos et al. (2012) is not appropriate for this purpose since many bright stars are lacking because of saturation. Therefore, we decided to build a new catalog by analyzing the archive HST/WFC3 images secured by using the F438W and F555W filters (proposal ID: 11628, PI: Noyola).

A total of six images have been analyzed: three images in the F438W filter with an exposure time of 420 s, and three in the F555W with an exposure time of 100 s. The photometric analysis has been performed using the software DAOPHOT (Stetson 1987). Briefly, in a first step the PSF in each image is modeled by using a large sub-sample ( $\sim 200$ ) of bright, isolated, and well-distributed stars. Then, a star search is performed in each image with a  $5\sigma$  threshold above the background level, and the PSF model previously found is fitted to all of these identified sources. Subsequently, we created as reference a master list including all the sources measured in at least half of the images acquired with the F555W filter. Using this master list we run the DAOPHOT/ALLFRAME package (Stetson 1994) to force the fit of the PSF model to the location of these sources in all the other images. For each of the identified stars, the magnitude values measured in the different filters were combined using DAOMATCH and DAOMASTER. The final catalog includes the instrumental coordinates, the mean magnitude in each filter, and the photometric errors for the detected sources. The instrumental magnitudes were then calibrated to the VEGAMAG photometric system by using the appropriate aperture corrections, zero-points and the procedure reported on the HST WFC3 website<sup>1</sup>. The instrumental positions were corrected for the effect of geometric distortions within the field of view, by applying the correction coefficients quoted in Bellini et al. (2011). Finally, the distortion-corrected positions have been placed onto the absolute coordinate system ( $\alpha$ ,  $\delta$ ) by cross-correlation with the *Gaia* DR3 catalog (Gaia Collaboration et al. 2023).

Even in this catalog, however, a few bright stars ( $\sim 10$ ) are saturated. To include them in the analysis, we thus performed a similar photometric analysis on two 2D MUSE images obtained by stacking the wavelength slices at 4840–4860 Å and 6060–6080 Å of each datacube. For each MUSE pointing we obtained a catalog with the instrumental positions and magnitudes of the detected stars. Then, the cross-correlation with the HST/WFC3 catalog discussed above allowed us to assign absolute coordinates and calibrated magnitudes to every MUSE star. We emphasize that we used the MUSE photometry only to recover the magnitude of the few bright stars that were saturated in the HST/WFC3 catalog. As the final reference catalog for PampelMuse, we thus adopted the HST/WFC3 catalog (which guarantees high astrometric precision and allows us to properly resolve stars even in the most crowded regions), with the addition of the MUSE measurements obtained for the few saturated sources.

Besides the reference catalog and the datacube, PampelMuse also requires in input an analytical PSF model, which is necessary for the source deblending. We selected the MAOPPY function (Férick et al. 2019) as PSF model, which accurately reproduces the typical double-component (core and halo) shape of the AO-corrected PSF in the MUSE/NFM observations (see Göttgens et al. 2021). Once the inputs are set, for each slice of the MUSE datacube, PampelMuse performs a PSF fitting using a sub-sample of stars, obtaining the wavelength dependencies of

the PSF parameters. At the same time, the software fits, for each slice, also the coordinate transformation from the reference catalog to the data. Then, these wavelength-dependent quantities are used to perform the deblending of all the sources present in the MUSE field of view, and extract the spectra.

### 3.2. The measure of radial velocities

To measure the radial velocity (RV) of the surveyed stars, we applied the same procedure described in Leanza et al. (2023, see also Pallanca et al. 2023), which uses the Doppler shifts of the Calcium Triplet lines (8450 – 8750 Å). The procedure needs a set of suitable synthetic spectra to be used as reference. We computed a library of synthetic spectra using the SYNTH code (Sbordone et al. 2004 and Kurucz 2005), adopting an  $\alpha$ -enhanced chemical mixture ( $[\alpha/\text{Fe}] = 0.4$  dex), the cluster metallicity  $[\text{Fe}/\text{H}] = -1.29$  dex (Carretta et al. 2009), and a set of atmospheric parameters (effective temperature and gravity) appropriate for the evolutionary stage of the targets, according to their position in the CMD. The spectra have been produced in the same wavelength range sampled by the observations, and convolved with a Gaussian profile to reproduce also the MUSE spectral resolution. Firstly, the observed spectra are normalized to the continuum, which is computed through a spline fitting of the spectrum in a proper wavelength range. The procedure compares the normalized observed spectra with each synthetic spectrum of the library, which is shifted in RV by steps of 0.1 km s<sup>-1</sup> in an adequate range of RV. For each velocity shift, and each template, the residuals between the observed spectrum and the synthetic one are computed. Then, for each target, the procedure finds the minimum standard deviation among all the residuals. This value is associated to a specific template and RV shift, therefore, the procedure derives, as a result, the best-fit synthetic spectrum (hence, an estimate of temperature and gravity), and the RV of the target. The procedure computes also the signal to noise ratio (S/N) of the spectra as the ratio between the average of the counts and their standard deviation in the spectral range 8000–9000 Å. The S/N of the targets is shown by the color scale in the left panel of Fig. 2.

We estimated the RV uncertainties ( $\epsilon_{\text{RV}}$ ) using Monte Carlo simulations. We generated  $\sim 9000$  simulated spectra with S/N between 10 and 90, and applied to these spectra the same procedure used for the observed ones, obtaining a relation to derive the RV uncertainties (for more details see Leanza et al. 2023). The errors obtained are of the order of 2 km s<sup>-1</sup> for the brightest stars, and increase to  $\sim 8$  km s<sup>-1</sup> for the faintest stars, as shown by the color scale of the CMD in the right panel of Figure 2.

### 3.3. Final MUSE catalog

In order to obtain a consistent catalog, we checked if the RV measurements were homogeneous among the different MUSE pointings. To this aim, exploiting the several overlapping fields in our data set, we compared the RV values measured for the stars in common between two adjacent overlapping regions, and we found offsets ranging from 2 to 4 km s<sup>-1</sup>. These offsets in the RV measurements might be introduced by variations in the wavelength calibration among the different pointings, since the MUSE observations were taken during different nights (in some cases in different months). To check the accuracy of the wavelength calibration and correct the offsets, we measured the RV from the Fraunhofer A telluric absorption bands (7570 – 7680 Å). We estimated the telluric RV for a sub-sample of targets with

<sup>1</sup> <https://www.stsci.edu/hst/instrumentation/wfc3/data-analysis/photometric-calibration/uv-vis-photometric-calibration>

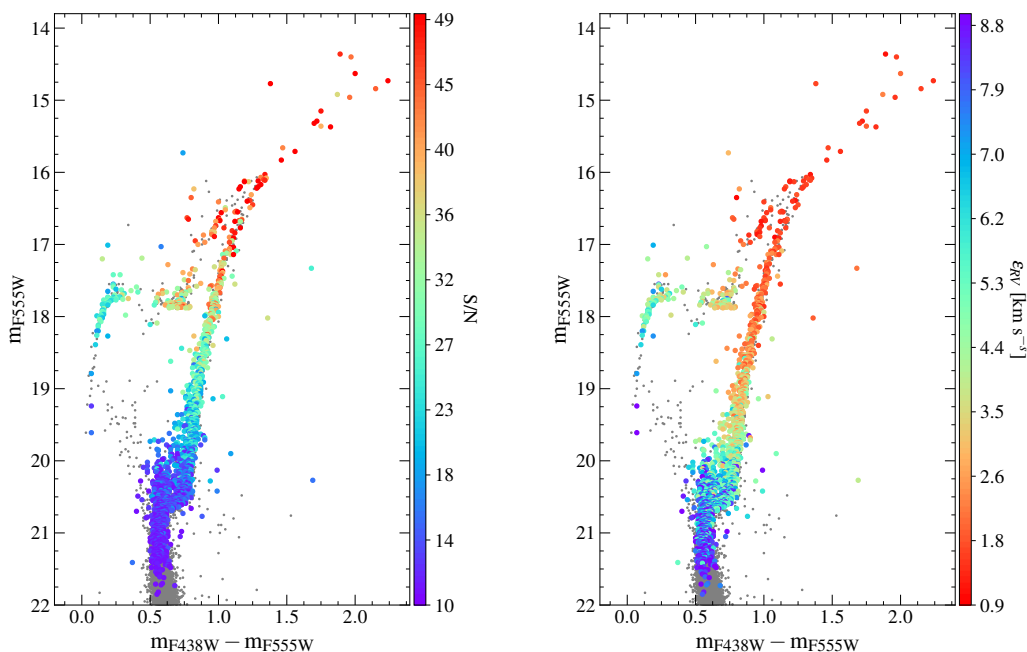


**Fig. 2.** CMD of M75 (gray dots) obtained from the HST/WFC3 photometric catalog described in Section 3. The large colored circles show the spectroscopic targets of the MUSE catalog (see Section 3.3), while the color scale in the left and right panels represents the S/N of the spectra, and the RV uncertainty, respectively.

$S/N > 20$  by using a procedure analogous to that adopted for the determination of the star RVs. In this case, a single template spectrum was adopted for each night. We generated the appropriate synthetics for the telluric absorption spectra by using the TAPAS tool<sup>2</sup> (Bertaux et al. 2014), setting the MUSE spectral range and resolution. For each pointing, we determined the average telluric RV, finding velocity zero-points from  $0.4 \text{ km s}^{-1}$  up to a maximum of  $3.3 \text{ km s}^{-1}$ . We then subtracted the value of each pointing from all the RV measurements of the stars in that field, in order to align the different pointings. The comparison of the RV values in two overlapping pointings after the correction finally showed a good agreement within the errors.

Moreover, we used the velocity measures ( $v_1$  and  $v_2$ ) of the targets in common between multiple pointings and their associated errors ( $\epsilon_1$  and  $\epsilon_2$ ) to check whether the estimated RV uncertainties are reliable. If the quantity

$$\delta v_{1,2} = \frac{v_1 - v_2}{\sqrt{\epsilon_1^2 + \epsilon_2^2}}, \quad (1)$$

results in a normal distribution with unit standard deviation, the uncertainties are properly estimated (see also Kamann et al. 2016). The resulting distribution is plotted in Fig. 3 and shows that our uncertainties have been properly estimated.

To construct the final catalog, only stars with  $S/N > 10$  have been considered, and for the targets with multiple exposures, the RV value was determined as the weighted mean of all the available measures, by using the individual errors as weights. The resulting MUSE catalog consists of 1872 RV measurements of individual stars. The CMD position of these stars is highlighted in Fig. 2 with large circles color-coded according to the S/N values and the RV uncertainties, in the left and right panels, respectively. Figure 4 shows the position of all the MUSE targets (gray

dots and colored circles) in the plane of the sky with respect to the cluster center, while their RVs as a function of the distance from the center and their RV distribution are plotted in Fig. 5 (left panel and empty histogram in the right panel, respectively).

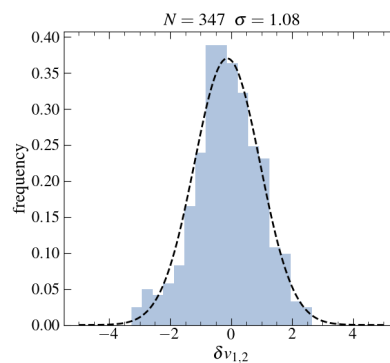


**Fig. 3.** Histogram of the values of  $\delta v_{1,2}$  obtained from Equation (1) for the stars with multiple exposures. The black dashed line represents the Gaussian fit to the histogram. Its standard deviation and the number of stellar pairs used are labeled at the top of the panel.

## 4. Results

For our kinematic study, we have selected only the (630) stars with the best RV measurements<sup>3</sup> with  $S/N > 20$  and RV error  $< 5 \text{ km s}^{-1}$ . The position in the plane of the sky of the selected sample is shown in Fig. 4 with large colored circles.

<sup>3</sup> The sample of bona fide RV measures with the corresponding errors is publicly available at: [http://www.cosmic-lab.eu/Cosmic-Lab/MIKIS\\_Survey.html](http://www.cosmic-lab.eu/Cosmic-Lab/MIKIS_Survey.html)

<sup>2</sup> <https://tapas.aeris-data.fr/en/home/>

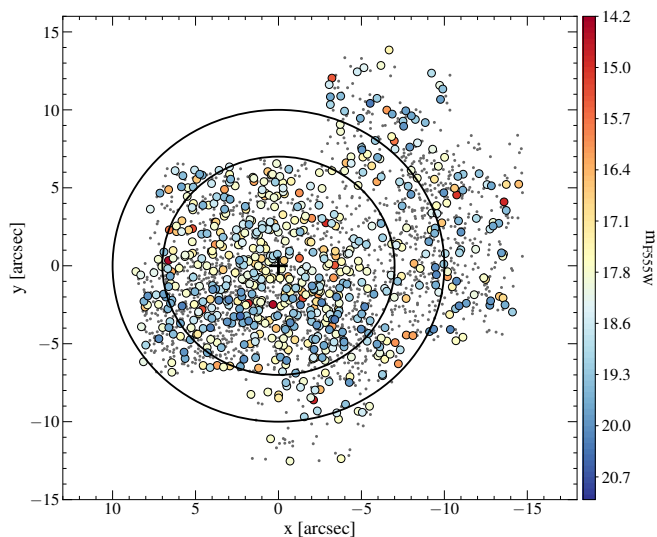


**Fig. 4.** Position of the MUSE targets in the plane of the sky, with respect to the cluster center (black cross, Contreras Ramos et al. 2012). The large colored circles mark the sample of stars that remain after the quality selection ( $S/N > 20$  and  $RV \text{ error} < 5 \text{ km s}^{-1}$ ; see Section 4) and that are used for the kinematic analysis, while the gray dots indicate the rejected targets. The color scale represents the  $m_{F555W}$  magnitude and the two circles are centered in the cluster center and have radii of  $7''$  and  $10''$ .

#### 4.1. Systemic velocity

The black dots and the gray shaded histogram in Fig. 5 show the RV distribution of the well-measured stars. As can be appreciated, the contamination from Galactic field sources is essentially null for this field of view. To properly determine the systemic velocity ( $V_{\text{sys}}$ ) of M75 we made the conservative choice of applying a  $2\sigma$ -clipping algorithm to the selected targets, thus removing possible outliers. Assuming a Gaussian distribution of the velocities, we estimated  $V_{\text{sys}}$  and its uncertainty by using a Maximum-Likelihood algorithm (Walker et al. 2006). The resulting value is  $V_{\text{sys}} = -189.5 \pm 0.3 \text{ km s}^{-1}$ . This result is in full agreement with the values quoted in Baumgardt & Hilker (2018,  $-188.6 \pm 0.9 \text{ km s}^{-1}$ ) and Harris (1996,  $-189.3 \pm 3.6 \text{ km s}^{-1}$ ), while it is consistent within  $\sim 2\sigma$  with that derived in Koch et al. (2018,  $-186.2 \pm 1.5 \text{ km s}^{-1}$ ).

#### 4.2. Systemic rotation

The internal kinematics of M75 has been little studied so far. In a previous work, Koch et al. (2018) found an indication of internal rotation in the outer region of the cluster. However, their analysis is based on a statistically poor sample (only 32 stars) of RV measurements. Taking advantage of our large data set, here we investigated the possible presence of ordered rotation in the central regions of the system.

For the analysis of the cluster's internal rotation, we have adopted a method often used in the literature (see, e.g., Leanza et al. 2023; Pallanca et al. 2023, and references therein; see also Cote et al. 1995; Bellazzini et al. 2012, for a full description of the method). Since the proper application of the procedure requires a uniform distribution of the RV measures in the plane of the sky, we limited the analysis to the sub-sample of (403) stars located within  $7''$  (corresponding to  $r < 1.4r_c$ , where  $r_c = 4.9''$  is the cluster core radius estimated in this work, see Section

6 and Fig. 7) from the center, thus avoiding some under-sampled regions (see Fig. 4).

The obtained results are discussed in the following and shown in Fig. 6. Following the adopted method, the RV sample is split into two sub-samples by a line passing through the center of the system, and with position angle (PA) varying anticlockwise from  $0^\circ$  (North) to  $180^\circ$  (South), by steps of  $10^\circ$ . The left panel of Fig. 6 shows the difference between the average velocity of the stars on each side of this line ( $\Delta V_{\text{mean}}$ ), as a function of PA. This draws an approximately sinusoidal pattern, which is a signal expected in the case of ordered rotation. From the maximum/minimum of the best-fit sine function (red solid line), we derived the rotation amplitude ( $A_{\text{rot}} = 0.8 \pm 0.3 \text{ km s}^{-1}$ ) as the half of this absolute value and the position angle of the rotation axis ( $PA_0 = 174 \pm 3^\circ$ ). In the middle panel of the same figure, the black dots show the measured RVs as a function of the projected distances from the rotation axis (XR), the red dashed line is the linear fit to the data performed by means of a least square algorithm. A rotating cluster should show a highly asymmetric distribution along two diagonally opposite quadrants. Finally, the cumulative velocity distributions of the two sub-samples of stars on each side of the rotation axis are shown in the right panel. A large difference between the two curves corresponds to a high probability of rotation. Therefore, to quantify the statistical significance of this difference, we have used three estimators. We computed the  $p$ -value of the Kolmogorov-Smirnov (KS) probability that the RV distributions of the two sub-samples are extracted from the same parent family ( $P_{\text{KS}}$ ), the  $t$ -Student probability that the two RV samples have different means ( $P_{\text{Stud}}$ ), and the significance level (in units of  $n\text{-}\sigma$ ) that the two means are different following a Maximum-Likelihood approach ( $n\text{-}\sigma_{\text{ML}}$ ), obtaining  $P_{\text{KS}} = 0.1$ ,  $P_{\text{Stud}} > 95\%$  and  $n\text{-}\sigma_{\text{ML}} = 2.9$ , respectively.

These results indicate a mild rotation signal in the region between  $0''$  and  $7''$ , with a maximum amplitude of  $\sim 1.0 \text{ km s}^{-1}$ . Although the statistical significance of this signal is not high, it is important to note that our estimate of the position angle of the rotation axis ( $PA_0 = 174 \pm 3^\circ$ ) is in good agreement with that found in Koch et al. (2018,  $PA_0 = -15 \pm 30^\circ$ , which corresponds to  $165^\circ$  according to our definition of PA) using a sample of 32 stars in the radial region  $20'' < r < 250''$ . Considering that the cluster regions explored in these two studies are complementary, we can conclude that there is a hint of ordered rotation in M75.

#### 4.3. Velocity dispersion profile

Given a sample of individual RV measurements, the dispersion of the RV distributions observed at different radial distances from the center provides the second velocity moment profile  $\sigma_{II}(r)$  of the cluster. This is related to the projected velocity dispersion profile  $\sigma_P(r)$  through the following expression:  $\sigma_P^2(r) = \sigma_{II}^2(r) - A_{\text{rot}}^2(r)$ . As discussed in the previous section, the amplitude of internal rotation (if any) is very small, and we can therefore assume that the velocity dispersion is reasonably approximated by the second velocity moment (i.e., hereafter  $\sigma_P(r) = \sigma_{II}(r)$ ).

To determine the velocity dispersion profile of M75 we divided the sample of bona fide RV measures in four concentric radial bins at increasing distance from the center, each one including more than 50 stars. We then applied a  $3\sigma$ -clipping algorithm to remove the outliers, and we determined the dispersion of the remaining RV measures through a Maximum-Likelihood



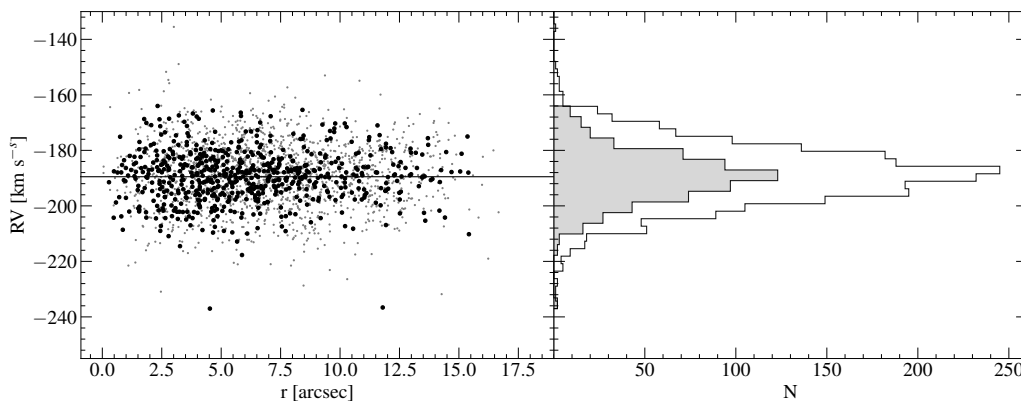


**Fig. 5.** *Left panel:* RVs of the final MUSE catalog (see Section 3.3) plotted as a function of the distance from the cluster center. The black dots highlight the sample of the well-measured stars (i.e., those with  $S/N > 20$  and  $RV \text{ error} < 5 \text{ km s}^{-1}$ ) that is used for the kinematic analysis. *Right panel:* the empty histogram shows the number distribution of the entire RV sample, while the gray histogram corresponds to the sub-sample of bona fide stars (black dots in the left panel).

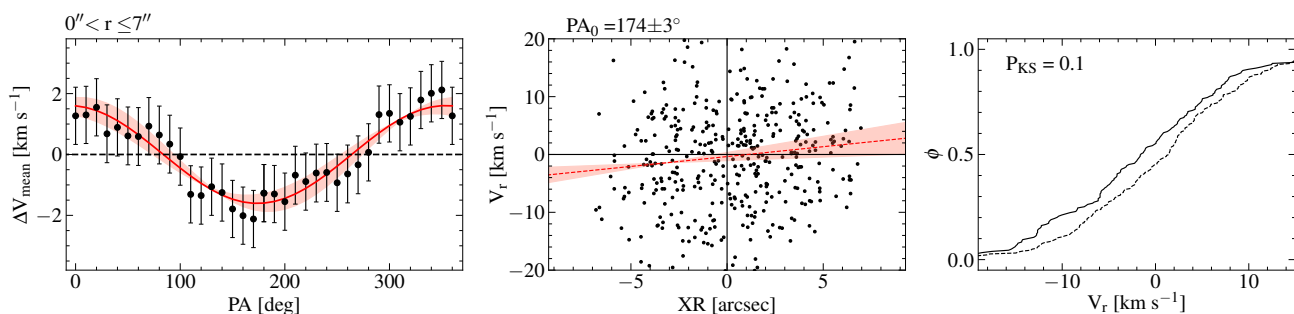


**Fig. 6.** Diagnostic diagrams of the rotation signal detected in M75, within  $7''$  from the cluster center. *Left panel:* difference between the mean RV on each side of an axis passing through the center as a function of the position angle (PA) of the axis itself. The red line is the sine function that best fits the observed pattern, while the red shaded region marks the confidence level at  $3\sigma$ . *Central panel:* distribution of the RVs referred to  $V_{\text{sys}}$  ( $V_r$ ), as a function of the projected distances from the rotation axis (XR) in arcseconds. The value of  $PA_0$  is labeled. The red dashed line is the least square fit to the data, and the red shaded area represents the  $1\sigma$  uncertainty of the linear fit. *Right panel:* cumulative  $V_r$  distributions for the stars with  $XR < 0$  (solid line) and for those with  $XR > 0$  (dotted line). The Kolmogorov-Smirnov probability that the two sub-samples are extracted from the same parent distribution is labeled.

approach, by maximizing the following likelihood:

$$\ln \mathcal{L} = -\frac{1}{2} \sum_i \left[ \frac{V_{r,i}^2}{(\sigma^2 + \epsilon_{v,i}^2)} + \ln(\sigma^2 + \epsilon_{v,i}^2) \right] \quad (2)$$

where  $V_{r,i} = RV_i - V_{\text{sys}}$  is the RV of the  $i^{\text{th}}$  star in the considered bin with respect to the cluster systemic velocity,  $\epsilon_{v,i}$  is its corresponding error,  $\sigma$  is the velocity dispersion in the bin, and the summation is made over all the stars included in the bin. We implemented the likelihood using a Markov Chain Monte Carlo (MCMC) approach, based on the emcee algorithm (Foreman-Mackey et al. 2013). From the posterior probability distribution function (PDF) obtained for the velocity dispersion in each bin, we derive the best-fit values of the dispersion as the PDF median, and its uncertainty from the 68% confidence interval. The velocity dispersion profile thus determined in the core of M75 is shown in the left panel of Fig. 7 (black circles) and listed in Table 2. The profile is roughly constant in the very center and starts to decrease at about  $6''$  from the center.

## 5. Distance, reddening and age estimate

The high quality of the available HST photometric data set offers the possibility of updated estimates of the cluster distance,

**Table 2.** Velocity dispersion profile of M75.

$r_i$ ["]	$r_e$ ["]	$r_m$ ["]	$N$	$\sigma_P \text{ km s}^{-1}$	$\epsilon_{\sigma_P} \text{ km s}^{-1}$
0.01	2.40	1.57	69	9.2	0.9
2.40	5.70	4.04	240	9.1	0.5
5.70	8.50	6.98	171	7.8	0.5
8.50	16.00	11.06	146	8.1	0.6

**Notes.** The table lists: the internal, external and mean radii of each adopted radial bin ( $r_i$ ,  $r_e$ , and  $r_m$ , respectively), the number of stars in the bin ( $N$ ), the projected velocity dispersion ( $\sigma_P$ ) and its uncertainty in the bin ( $\epsilon_{\sigma_P}$ ).

reddening and age. In fact, the positions of various evolutionary sequences in the CMD of an old stellar population provide useful references to constrain these parameters through the comparison with theoretical models (see examples in Saracino et al. 2019; Cadelano et al. 2019, 2020a,b; Deras et al. 2023; Massari et al. 2023). In particular, the vertical portion of the CMD at the base of the RGB, and the horizontal portion of the horizontal branch (HB) are sensitive, respectively, to the color excess and the cluster distance, independently of the (old) age of the popu-

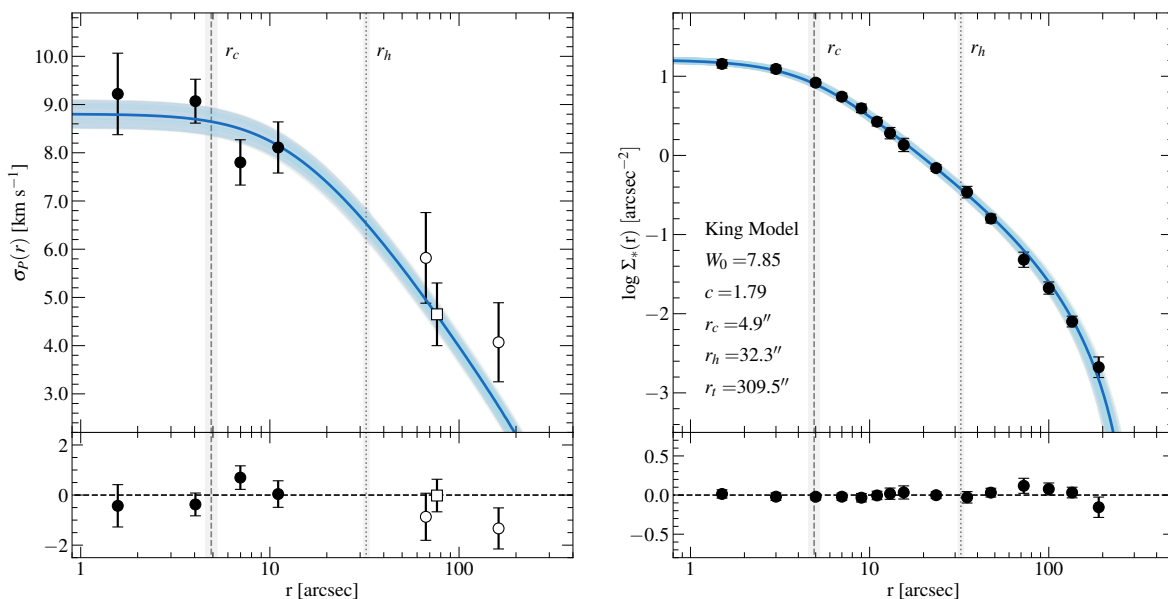


**Fig. 7.** *Left panel:* Projected velocity dispersion profile of M75 obtained from the MUSE RV measures discussed in this work (black circles). The values of the line-of-sight velocity dispersion quoted in the online repository <https://people.smp.uq.edu.au/HolgerBaumgardt/globular/>, and the one obtained from *Gaia* proper motions (Vasiliev & Baumgardt 2021) rescaled to the distance estimated in Section 5 (see Table 3), are also plotted as empty circles and empty square, respectively. The blue line corresponds to the best-fit King model derived from the simultaneous fit to this profile and the density profile shown in the right panel. The shaded regions show the  $1\sigma$  uncertainty on the best-fit. The dashed and dotted vertical lines mark the derived core radius ( $r_c$ ) and half-mass radius ( $r_h$ ), respectively. The bottom panel shows the residuals between the King model and the observations. *Right panel:* Projected density profile from resolved star counts obtained by Contreras Ramos et al. (2012, black circles). The meaning of the lines, shaded region, and bottom panel is as in the left panel. The values of the best-fit central dimensionless potential ( $W_0$ ), concentration parameter ( $c$ ),  $r_c$ ,  $r_h$ , and tidal radius ( $r_t$ ) are labeled in the panel.

lation, while the main sequence turnoff and the sub-giant branch regions are the most age-sensitive evolutionary sequences.

To determine first-guess estimates of color excess and distance, we extracted from the BaSTI-IAC database (Pietrinferni et al. 2021) a 12 Gyr old isochrone with appropriate metallicity ( $[\text{Fe}/\text{H}] = -1.3$  dex; Carretta et al. 2009) standard helium mass fraction ( $Y = 0.25$ ), and  $[\alpha/\text{Fe}] = +0.4$  (which is the typical value for Galactic GCs at this metallicity). We searched for the shifts in color and magnitude necessary to superpose the model to the samples of stars selected at the base of the RGB in the magnitude range  $19 < m_{F555W} < 20$  and in the HB portion at  $0.5 < (m_{F438W} - m_{F555W}) < 0.8$ . A reasonable reproduction of the observed loci is obtained by adopting a color excess  $E(B - V) = 0.16$  and a distance modulus  $(m - M)_0 = 16.7$ . Starting from these first-guess values, we then determined the best-fit cluster age, distance, and reddening through the isochrone fitting technique, following a Bayesian procedure similar to that used in many previous works (see, e.g., Saracino et al. 2019; Cadelano et al. 2019, 2020b; Deras et al. 2023; Massari et al. 2023). This approach consists in comparing the observed CMD with a set of isochrones, simultaneously exploring suitable grids for the age, distance modulus and color excess. We extracted a set of isochrones from the BaSTI-IAC repository (Pietrinferni et al. 2021) computed assuming the same chemical composition quoted above, and ages ranging between 9 Gyr and 15 Gyr, in steps of 0.2 Gyr. The comparison between the observed CMD and the isochrones has been performed by adopting an MCMC technique, assuming a Gaussian likelihood function (see equations 2 and 3 in Cadelano et al. 2020b). To properly constrain the level of the HB, we also included a term in the likelihood function to minimize the distance in magnitude between the zero-age horizontal branch of the models and the level of the red por-

tion of the observed HB. We used the emcee code (Foreman-Mackey et al. 2013) to sample the posterior probability distribution in the parameter space. A flat prior has been assumed for the explored age range. To convert the isochrone absolute magnitudes to the observational plane, we adopted values of the color excess and distance modulus following Gaussian prior distributions peaked at the first-guess values quoted above. To improve the definition of the main sequence turnoff and sub-giant branch evolutionary sequences in the CMD (in the magnitude range  $19.5 < m_{F555W} < 21.5$ ), we considered only stars at distances larger than  $25''$  from the cluster center.

The best-fit values correspond to the 50th percentile of the posterior probability distribution of each parameter. Since we have constrained the HB level and fixed the metallicity of the models, the formal  $1\sigma$  uncertainties obtained from the posterior probability distributions of the MCMC are underestimated. Hence, we have included the uncertainty on the HB level in the propagation of the errors and adopted the conservative  $1\sigma$  uncertainties listed below. The best-fit values of the derived quantities are  $E(B - V) = 0.17 \pm 0.02$ ,  $(m - M)_0 = 16.64 \pm 0.05$  (corresponding to a distance of  $21.3 \pm 0.5$  kpc), and an age of  $11.0 \pm 0.4$  Gyr (see also Table 3). The resulting best-fit isochrone is shown in Fig. 8. Assuming a larger metallicity ( $[\text{Fe}/\text{H}] = -1.2$  dex; see Kacharov et al. 2013), the isochrone fit slightly worsens, but it still provides values of the three parameters that are well consistent with the best-fit ones within the errors. While the estimated reddening is fully consistent with that reported in the literature (Harris 1996), the distance of the cluster is slightly larger than the previous values (20.9 kpc in Harris 1996, 20.52 kpc in Baumgardt & Vasiliev 2021).

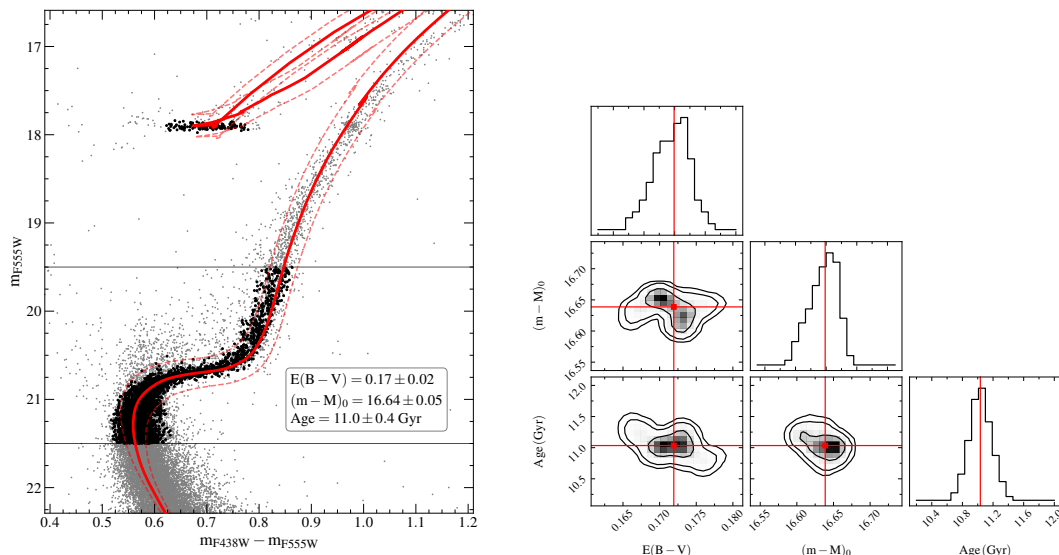


**Fig. 8.** *Left panel:* CMD of M75 (gray dots) with the best-fit BaSTI isochrone computed with  $[\text{Fe}/\text{H}] = -1.3$  dex plotted as a red solid line. The dashed red isochrones represent the uncertainties on the parameters. The black circles mark the stars used for the isochrone fitting procedure. The resulting best-fit values of color excess, distance modulus and age are labeled. *Right panel:* corner plots showing the one- and two-dimensional projections of the posterior probability distributions for all the parameters derived from the MCMC method. The contours correspond to the 68%, 95%, and 99% confidence levels.

## 6. Discussion and Conclusions

In this paper we presented a new result of the MIKIS survey: the first kinematic exploration of the central regions of M75 (NGC 6864), a GC orbiting the outer halo of the Milky Way. By using a set of AO-corrected MUSE/NFM observations, we obtained a sample of  $\sim 1900$  RV measurements of individual stars located within  $16''$  ( $\sim 3r_c$ ) from the cluster center. From a sub-sample of 630 well measured stars (i.e., with MUSE spectra having  $S/N > 20$  and with RV uncertainties smaller than  $5 \text{ km s}^{-1}$ ), we determined the systemic velocity of the cluster ( $V_{\text{sys}} = -189.5 \pm 0.3 \text{ km s}^{-1}$ ) and the innermost portion ( $r < 16''$ ) of its velocity dispersion profile. By taking advantage of the high photometric quality of the HST/WFC3 catalog, we also determined updated estimates of the cluster distance, reddening and age (see Table 3).

By using a set of single-mass, spherical, isotropic and non-rotating King models (King 1966),<sup>4</sup> We simultaneously fitted the velocity dispersion profile obtained by combining the one derived in this work with literature values (see left panel of Fig. 7), and the projected density profile obtained from the resolved star counts in Contreras Ramos et al. (2012). The approximation of single-mass and non-rotating models is legitimate by the fact that both profiles have been obtained from samples of stars with approximately the same mass (main sequence turnoff and giant stars), and that the rotation signal is negligible in this system (see Section 4.2).

The best-fit solution has been determined by using an MCMC method through the emcee algorithm (Foreman-Mackey et al. 2013). We assumed a  $\chi^2$  likelihood and uniform priors on the parameters of the fit (i.e., the King concentration parameter  $c$ ,

<sup>4</sup> The King models (King 1966) are a single-parameter family of dynamical models, meaning that their shape is univocally determined by the dimensionless parameter  $W_0$ , which is proportional to the gravitational potential at the center of the system, or alternatively, by the concentration parameter  $c \equiv \log(r_t/r_0)$ , where  $r_t$  and  $r_0$  are the tidal and the King radii of the model, respectively. Other characteristic parameters of the cluster structure are the core radius  $r_c$  and the half-mass radius  $r_h$ .

the core radius  $r_c$ , the value of the central density, and the central velocity dispersion  $\sigma_0$ ). For each parameter, the 50-th percentile of the PDF has been adopted as best-fit value, while the 16-th and 84-th percentiles have been used to determine the  $1\sigma$  uncertainty. The fitting procedure provides a best-fit King model characterized by  $W_0 = 7.85 \pm 0.1$ , concentration  $c = 1.79 \pm 0.03$ , core radius  $r_c = 4.9''^{+0.4}_{-0.3}$ , half-mass radius  $r_h = 32.3''^{+1.2}_{-1.0}$ , tidal radius  $r_t = 309.5''^{+11.9}_{-10.7}$ , and a central velocity dispersion  $\sigma_0 = 8.8 \pm 0.3 \text{ km s}^{-1}$ . Figure 7 shows the resulting best-fit King model (blue solid lines) overplotted to the observed velocity dispersion and density profiles (left and right panels, respectively). The bottom panels show the residuals between the model and the observations. The best-fit values and the uncertainties of each parameter are listed in Table 3.

The value of the central velocity dispersion estimated in this work is significantly smaller than those quoted in Koch et al. (2018,  $\sigma_0 = 14.1^{+2.4}_{-2.0} \text{ km s}^{-1}$ ), and in Baumgardt & Hilker (2018,  $\sigma_0 = 11.8 \text{ km s}^{-1}$ , which has been updated to  $12.3 \text{ km s}^{-1}$  in the online version). However, the literature values are both extrapolated from the fit to observational data that are confined to the cluster outer regions, while, for the first time in this work, the central portion of the velocity dispersion profile is directly constrained by observations. In particular, Koch et al. (2018) fitted a Plummer model (see their eq. 3) to a sample of just 32 stars located between  $\sim 20''$  and  $250''$  from the center, while Baumgardt & Hilker (2018) used N-body simulations and a velocity dispersion profile with the innermost radial bin located at  $\sim 70''$  from the center (see empty circles in Fig. 7). It is also worth keeping in mind that our analysis is mainly based on RGB stars that are slightly more massive ( $\sim 0.8M_\odot$ ) than the average cluster stars ( $\sim 0.3M_\odot$ ), while the central velocity dispersion estimated by Baumgardt & Hilker (2018) from N-body simulations is weighted by stellar masses. Taking into account the effects of energy equipartition and mass segregation, this could partially justify the smaller value estimated in this work. Indeed, the analyses conducted so far clearly suggest that M75 is a highly dynamically evolved stellar system. The central relaxation time



**Table 3.** Parameters of M75 determined in this work.

Parameter	Estimated Value
Color excess	$E(B - V) = 0.17 \pm 0.02$
Distance modulus	$(m - M)_0 = 16.64 \pm 0.05$
Cluster distance	$d = 21.3 \pm 0.5$ kpc
Age	$11.0 \pm 0.4$ Gyr
Dimensionless central potential	$W_0 = 7.85 \pm 0.1$
Concentration parameter	$c = 1.79 \pm 0.03$
Core radius	$r_c = 4.90''^{+0.4}_{-0.3}$
Half-mass radius	$r_h = 32.3''^{+1.2}_{-1.0}$
Tidal radius	$r_t = 309.5''^{+11.9}_{-10.7}$
Systemic velocity	$V_{\text{sys}} = -189.5 \pm 0.3$ km s <sup>-1</sup>
Central velocity dispersion	$\sigma_0 = 8.8 \pm 0.3$ km s <sup>-1</sup>
Total mass	$M = 2.5 \pm 0.2 \times 10^5 M_\odot$

( $\log t_{rc}/\text{yr} = 8.0$  Lanzoni et al. 2016) compared to the cluster age (11 Gyr; see Section 5) indicates that the system has undergone several relaxations so far. In addition, the large value of the BSS segregation level (the  $A_{rh}^+$  parameter) empirically confirms the high level of dynamical evolution and central mass segregation in this cluster (see, Lanzoni et al. 2016; Ferraro et al. 2023a). Hence, RGB stars are more centrally segregated than the average and their central velocity dispersion is lower than the mass-weighted value.

As motivated above, M75 can be well approximated by a single-mass, spherical, isotropic, and non-rotating King model (King 1966). Under this assumption, the total mass of the system can be estimated from the value of  $\sigma_0$  following equation (3) in Majewski et al. (2003, see also Richstone & Tremaine 1986):  $M = 1.66r_c\mu/\beta$ , where  $\mu$  is a polynomial function of the King concentration parameter (see eq. 8 in Djorgovski 1993), and  $\beta = 1/\sigma_0^2$ . The resulting total mass is  $M = 2.5 \pm 0.2 \times 10^5 M_\odot$ , where the uncertainty has been estimated through Monte Carlo simulations (see Leanza et al. 2022; Pallanca et al. 2023). This value is a factor of two smaller than the value derived in Baumgardt & Hilker (2018,  $5.86 \pm 1.24 \times 10^5 M_\odot$ ), mainly due to the significant difference in the values of  $\sigma_0$ , and also because of the different assumptions (e.g., from Section 5, we adopted a distance of 21.3 kpc, while Baumgardt & Hilker 2018 use 20.5 kpc) and the different methods used in the two works.

Finally, using the selected sample of MUSE RVs, we investigated the systemic rotation in the innermost region of the cluster ( $r < 7''$ , corresponding to  $r < 1.4r_c$ ). We found just a weak hint of rotation ( $A_{\text{rot}} \sim 1$  km s<sup>-1</sup>) with a position angle of the rotation axis  $\text{PA}_0 = 174 \pm 3^\circ$ . It is intriguing to note that the value of  $\text{PA}_0$  obtained in the present paper is fully consistent with that of the rotation signal detected by Koch et al. (2018) in the outer regions. Thus, in spite of the limitation of the two samples and the low statistical significance of both detections, there is now a stronger hint of internal rotation in M75 that deserves further investigation.

*Acknowledgements.* This work is part of the project *Cosmic-Lab* at the Physics and Astronomy Department "A. Righi" of the Bologna University (<http://www.cosmic-lab.eu/Cosmic-Lab/Home.html>).

## References

Arsenault, R., Madec, P.-Y., Hubin, N., et al. 2008, Proc. SPIE, 7015, 701524

- Bacon, R., Accardo, M., Adjali, L., et al. 2010, Proc. SPIE, 7735, 773508  
 Bailyn, C. D. 1995, ARA&A, 33, 133  
 Baumgardt, H. & Hilker, M. 2018, MNRAS, 478, 1520  
 Baumgardt, H. & Vasiliev, E. 2021, MNRAS, 505, 5957  
 Bellazzini, M., Bragaglia, A., Carretta, E., et al. 2012, A&A, 538, A18  
 Bellini, A., Anderson, J., & Bedin, L. R. 2011, PASP, 123, 622  
 Bertaux, J. L., Lallement, R., Ferron, S., et al. 2014, A&A, 564, A46  
 Bianchini, P., Varri, A. L., Bertin, G., et al. 2013, ApJ, 772, 67  
 Billi, A., Ferraro, F. R., Mucciarelli, A., et al. 2023, ApJ, 956, 124  
 Boberg, O. M., Vesperini, E., Friel, E. D., et al. 2017, ApJ, 841, 114  
 Cadelano, M., Ransom, S. M., Freire, P. C. C., et al. 2018, ApJ, 855, 125  
 Cadelano, M., Ferraro, F. R., Istrate, A. G., et al. 2019, ApJ, 875, 25  
 Cadelano, M., Chen, J., Pallanca, C., et al. 2020, ApJ, 905, 63  
 Cadelano, M., Saracino, S., Dalessandro, E., et al. 2020, ApJ, 895, 54  
 Cadelano, M., Pallanca, C., Dalessandro, E., et al. 2023, A&A, 679, L13  
 Carretta, E., Bragaglia, A., Gratton, R., et al. 2009, A&A, 508, 695  
 Contreras Ramos, R., Ferraro, F. R., Dalessandro, E., et al. 2012, ApJ, 748, 91  
 Cote, P., Welch, D. L., Fischer, P., et al. 1995, ApJ, 454, 788  
 Crociati, C., Valentí, E., Ferraro, F. R., et al. 2023, ApJ, 951, 17  
 Dalessandro, E., Lanzoni, B., Ferraro, F. R., et al. 2008, ApJ, 677, 1069  
 Dalessandro, E., Salaris, M., Ferraro, F. R., et al. 2013a, MNRAS, 430, 459  
 Dalessandro, E., Ferraro, F. R., Massari, D., et al. 2013b, ApJ, 778, 135  
 Dalessandro, E., Massari, D., Bellazzini, M., et al. 2014, ApJ, 791, L4  
 Dalessandro, E., Lapenna, E., Mucciarelli, A., et al. 2016, ApJ, 829, 77  
 Dalessandro, E., Raso, S., Kamann, S., et al. 2021, MNRAS, 506, 813  
 Dalessandro, E., Crociati, C., Cignoni, M., et al. 2022, ApJ, 940, 170  
 Deras, D., Cadelano, M., Ferraro, F. R., et al. 2023, ApJ, 942, 104  
 Deras, D., Cadelano, M., Lanzoni, B., et al. 2024, A&A, 681, A38  
 Dresbach, F., Massari, D., Lanzoni, B., et al. 2022, ApJ, 928, 47  
 Djorgovski, S. 1993, Structure and Dynamics of Globular Clusters, 50, 373  
 Fabricius, M. H., Noyola, E., Rukdee, S., et al. 2014, ApJ, 787, L26  
 Ferraro, F. R., Fusi Pecci, F., & Buonanno, R. 1992, MNRAS, 256, 376  
 Ferraro, F. R., Paltrinieri, B., Fusi Pecci, F., et al. 1997, ApJ, 484, L145  
 Ferraro, F. R., Paltrinieri, B., Rood, R. T., et al. 1999, ApJ, 522, 983  
 Ferraro, F. R., Possenti, A., D'Amico, N., et al. 2001, ApJ, 561, L93  
 Ferraro, F. R., Sills, A., Rood, R. T., et al. 2003, ApJ, 588, 464  
 Ferraro, F. R., Dalessandro, E., Mucciarelli, A., et al. 2009a, Nature, 462, 483  
 Ferraro, F. R., Beccari, G., Dalessandro, E., et al. 2009b, Nature, 462, 1028  
 Ferraro, F. R., Lanzoni, B., Dalessandro, E., et al. 2012, Nature, 492, 393  
 Ferraro, F. R., Massari, D., Dalessandro, E., et al. 2016, ApJ, 828, 75  
 Ferraro, F. R., Lanzoni, B., Raso, S., et al. 2018a, ApJ, 860, 36  
 Ferraro, F. R., Mucciarelli, A., Lanzoni, B., et al. 2018b, ApJ, 860, 50  
 Ferraro, F. R., Mucciarelli, A., Lanzoni, B., et al. 2018c, The Messenger, 172, 18  
 Ferraro, F. R., Lanzoni, B., Dalessandro, E., et al. 2019, Nature Astronomy, 3, 1149  
 Ferraro, F. R., Lanzoni, B., & Dalessandro, E. 2020, Rendiconti Lincei. Scienze Fisiche e Naturali, 31, 19  
 Ferraro, F. R., Pallanca, C., Lanzoni, B., et al. 2021, Nature Astronomy, 5, 311  
 Ferraro, F. R., Lanzoni, B., Vesperini, E., et al. 2023a, ApJ, 950, 145  
 Ferraro, F. R., Mucciarelli, A., Lanzoni, B., et al. 2023b, Nature Communications, 14, 2584  
 Fétick, R. J. L., Fusco, T., Neichel, B., et al. 2019, A&A, 628, A99  
 Foreman-Mackey, D., Hogg, D. W., Lang, D., et al. 2013, PASP, 125, 306  
 Freudling, W., Romaniello, M., Bramich, D. M., et al. 2013, A&A, 559, A96  
 Gaia Collaboration, Vallenari, A., Brown, A. G. A., et al. 2023, A&A, 674, A1  
 Götgens, F., Kamann, S., Baumgardt, H., et al. 2021, MNRAS, 507, 4788  
 Harris, W. E. 1996, 2010 edition, AJ, 112, 1487  
 Kacharov, N., Koch, A., & McWilliam, A. 2013, A&A, 554, A81  
 Kamann, S., Husser, T.-O., Brinchmann, J., et al. 2016, A&A, 588, A149  
 Kamann, S., Wisotzki, L., & Roth, M. M. 2013, A&A, 549, A71  
 King, I. R. 1966, AJ, 71, 64  
 Koch, A., Hanke, M., & Kacharov, N. 2018, A&A, 616, A74  
 Kurucz, R. L. 2005, Memorie della Societa Astronomica Italiana Supplementi, 8, 14  
 Ibata, R., Bellazzini, M., Chapman, S. C., et al. 2009, ApJ, 699, L169  
 Lane, R. R., Kiss, L. L., Lewis, G. F., et al. 2009, MNRAS, 400, 917  
 Lanzoni, B., Dalessandro, E., Ferraro, F. R., et al. 2007, ApJ, 668, L139  
 Lanzoni, B., Ferraro, F. R., Dalessandro, E., et al. 2010, ApJ, 717, 653  
 Lanzoni, B., Mucciarelli, A., Origlia, L., et al. 2013, ApJ, 769, 107  
 Lanzoni, B., Ferraro, F. R., Alessandrini, E., et al. 2016, ApJ, 833, L29  
 Lanzoni, B., Ferraro, F. R., Mucciarelli, A., et al. 2018a, ApJ, 861, 16  
 Lanzoni, B., Ferraro, F. R., Mucciarelli, A., et al. 2018b, ApJ, 865, 11  
 Lanzoni, B., Ferraro, F. R., Dalessandro, E., et al. 2019, ApJ, 887, 176  
 Leanza, S., Pallanca, C., Ferraro, F. R., et al. 2022, ApJ, 929, 186  
 Leanza, S., Pallanca, C., Ferraro, F. R., et al. 2023, ApJ, 944, 162  
 Libralato, M., Bellini, A., van der Marel, R. P., et al. 2018, ApJ, 861, 99  
 Massari, D., Mucciarelli, A., Ferraro, F. R., et al. 2014, ApJ, 791, 101  
 Massari, D., Aguado-Agelet, F., Monelli, M., et al. 2023, A&A, 680, A20  
 Majewski, S. R., Skrutskie, M. F., Weinberg, M. D., et al. 2003, ApJ, 599, 1082  
 Martin, N. F., Ibata, R. A., Chapman, S. C., et al. 2007, MNRAS, 380, 281  
 Miocchi, P., Lanzoni, B., Ferraro, F. R., et al. 2013, ApJ, 774, 151

- Origlia, L., Ferraro, F. R., Fusi Pecci, F., et al. 1997, A&A, 321, 859  
Origlia, L., Ferraro, F. R., Fusi Pecci, F., et al. 2002, ApJ, 571, 458  
Origlia, L., Ferraro, F. R., Bellazzini, M., et al. 2003, ApJ, 591, 916  
Origlia, L., Rich, R. M., Ferraro, F. R., et al. 2011, ApJ, 726, L20  
Origlia, L., Massari, D., Rich, R. M., et al. 2013, ApJ, 779, L5  
Origlia, L., Mucciarelli, A., Fiorentino, G., et al. 2019, ApJ, 871, 114  
Pallanca, C., Dalessandro, E., Ferraro, F. R., et al. 2010, ApJ, 725, 1165  
Pallanca, C., Dalessandro, E., Ferraro, F. R., et al. 2013, ApJ, 773, 122  
Pallanca, C., Ransom, S. M., Ferraro, F. R., et al. 2014, ApJ, 795, 29  
Pallanca, C., Beccari, G., Ferraro, F. R., et al. 2017, ApJ, 845, 4  
Pallanca, C., Lanzoni, B., Ferraro, F. R., et al. 2021, ApJ, 913, 137  
Pallanca, C., Leanza, S., Ferraro, F. R., et al. 2023, ApJ, 950, 138  
Paresce, F., de Marchi, G., & Ferraro, F. R. 1992, Nature, 360, 46  
Pietrinferni, A., Hidalgo, S., Cassisi, S., et al. 2021, ApJ, 908, 102  
Pooley, D., Lewin, W. H. G., Anderson, S. F., et al. 2003, ApJ, 591, L131  
Pryor, C. & Meylan, G. 1993, Structure and Dynamics of Globular Clusters, 50, 357  
Ransom, S. M., Hessels, J. W. T., Stairs, I. H., et al. 2005, Science, 307, 892  
Raso, S., Libralato, M., Bellini, A., et al. 2020, ApJ, 895, 15  
Richstone, D. O. & Tremaine, S. 1986, AJ, 92, 72  
Saracino, S., Dalessandro, E., Ferraro, F. R., et al. 2015, ApJ, 806, 152  
Saracino, S., Dalessandro, E., Ferraro, F. R., et al. 2019, ApJ, 874, 86  
Sbordone, L., Bonifacio, P., Castelli, F., et al. 2004, Memorie della Societa Astronomica Italiana Supplementi, 5, 93  
Sollima, A., Bellazzini, M., Smart, R. L., et al. 2009, MNRAS, 396, 2183  
Stetson, P. B. 1994, PASP, 106, 250  
Stetson, P. B. 1987, PASP, 99, 191  
Ströbele, S., La Penna, P., Arsenault, R., et al. 2012, Proc. SPIE, 8447, 844737  
Valenti, E., Ferraro, F. R., & Origlia, L. 2010, MNRAS, 402, 1729  
Vasiliev, E. & Baumgardt, H. 2021, MNRAS, 505, 5978  
Walker, M. G., Mateo, M., Olszewski, E. W., et al. 2006, AJ, 131, 2114  
Weilbacher, P. M., Palsa, R., Streicher, O., et al. 2020, A&A, 641, A28